



Article

Predicting Gross Primary Productivity under Future Climate Change for the Tibetan Plateau Based on Convolutional Neural Networks

Meimei Li ¹, Zhongzheng Zhu ² , Weiwei Ren ^{2,*} and Yingzheng Wang ³

¹ State Key Laboratory of Biocontrol, School of Ecology, Shenzhen Campus of Sun Yat-sen University, Shenzhen 518107, China; limm35@mail.sysu.edu.cn

² National Tibetan Plateau Data Center (TPDC), State Key Laboratory of Tibetan Plateau Earth System Science, Environment and Resources (TPESER), Institute of Tibetan Plateau Research, Chinese Academy of Sciences, Beijing 100101, China; zhuzz@itpcas.ac.cn

³ College of Earth and Environmental Sciences, Lanzhou University, Lanzhou 730000, China; wangyzh20@lzu.edu.cn

* Correspondence: renweiwei@itpcas.ac.cn

Abstract: Gross primary productivity (GPP) is vital for ecosystems and the global carbon cycle, serving as a sensitive indicator of ecosystems' responses to climate change. However, the impact of future climate changes on GPP in the Tibetan Plateau, an ecologically important and climatically sensitive region, remains underexplored. This study aimed to develop a data-driven approach to predict the seasonal and annual variations in GPP in the Tibetan Plateau up to the year 2100 under changing climatic conditions. A convolutional neural network (CNN) was employed to investigate the relationships between GPP and various environmental factors, including climate variables, CO₂ concentrations, and terrain attributes. This study analyzed the projected seasonal and annual GPP from the Coupled Model Intercomparison Project Phase 6 (CMIP6) under four future scenarios: SSP1–2.6, SSP2–4.5, SSP3–7.0, and SSP5–8.5. The results suggest that the annual GPP is expected to significantly increase throughout the 21st century under all future climate scenarios. By 2100, the annual GPP is projected to reach 1011.98 Tg C, 1032.67 Tg C, 1044.35 Tg C, and 1055.50 Tg C under the four scenarios, representing changes of 0.36%, 4.02%, 5.55%, and 5.67% relative to 2021. A seasonal analysis indicates that the GPP in spring and autumn shows more pronounced growth under the SSP3–7.0 and SSP5–8.5 scenarios due to the extended growing season. Furthermore, the study identified an elevation band between 3000 and 4500 m that is particularly sensitive to climate change in terms of the GPP response. Significant GPP increases would occur in the east of the Tibetan Plateau, including the Qilian Mountains and the upper reaches of the Yellow and Yangtze Rivers. These findings highlight the pivotal role of climate change in driving future GPP dynamics in this region. These insights not only bridge existing knowledge gaps regarding the impact of future climate change on the GPP of the Tibetan Plateau over the coming decades but also provide valuable guidance for the formulation of climate adaptation strategies aimed at ecological conservation and carbon management.

Keywords: Tibetan Plateau; gross primary productivity; climate change; spatiotemporal variation; convolutional neural networks



Citation: Li, M.; Zhu, Z.; Ren, W.; Wang, Y. Predicting Gross Primary Productivity under Future Climate Change for the Tibetan Plateau Based on Convolutional Neural Networks.

Remote Sens. **2024**, *16*, 3723.

<https://doi.org/10.3390/rs16193723>

Academic Editor: Jeroen Meersmans

Received: 20 August 2024

Revised: 24 September 2024

Accepted: 4 October 2024

Published: 7 October 2024



Copyright: © 2024 by the authors. Licensee MDPI, Basel, Switzerland. This article is an open access article distributed under the terms and conditions of the Creative Commons Attribution (CC BY) license (<https://creativecommons.org/licenses/by/4.0/>).

1. Introduction

The ecosystems of the Tibetan Plateau are highly sensitive to climate change and play a significant role in China's efforts to achieve its "carbon neutrality" goals [1]. Gross primary productivity (GPP) is a major component of the carbon cycle, which plays an essential role in regulating the Earth's carbon balance [2,3]. Even minor fluctuations in GPP can substantially influence the ecosystem's carbon sequestration capacity and subsequent climate

feedback [1,4]. However, increasing evidence shows that the global CO₂ emissions continue to rise [5,6]; this trajectory will lead to strong warming scenarios, exceeding 4 °C by the end of this century, with ongoing warming thereafter [7]. Therefore, gaining a comprehensive understanding of the impacts of climate change on the GPP of the Tibetan Plateau, and predicting its future variations under different climate scenarios, is essential in developing targeted emission reduction and carbon sequestration strategies. This knowledge will provide a robust scientific basis for the achievement of carbon neutrality goals.

Over the past few decades, considerable studies have focused on assessing the impact of climate change on GPP. Common methods for the estimation of GPP typically involve process-based physical models that integrate physiological and ecological mechanisms related to vegetation growth, such as radiative transfer, photosynthesis, and respiration [8,9]. These models are generally categorized as either land surface models (LSMs) or Earth system models (ESMs). LSMs are rooted in theories and hypotheses about ecosystem functioning and include various mechanistic or empirical sub-models to simulate fluctuations in ecosystem energy, water, and carbon fluxes [10,11]. ESMs, on the other hand, consider physical, chemical, and biological processes within the Earth's ecosystems to model carbon cycle interactions between the biosphere and atmosphere [12,13]. The strength of process-based physical models lies in their capacity to account for multiple processes and provide spatially continuous GPP estimates over long time series. For instance, Li et al. [10] evaluated the performance of the second version of the Beijing Climate Center Atmosphere–Vegetation Interaction Model in simulating the GPP across various spatial and temporal scales. However, these models also have limitations. The inclusion of numerous physical processes introduces uncertainties in the model parameters and reduces the adaptability to large-scale regions. For example, Zhang et al. [14] assessed the GPP simulation results of seven general circulation models (GCMs) and found that no single climate model accurately captured the interannual variation in GPP and ecosystem responses to climate change, particularly in the Tibetan Plateau. Consequently, there is significant uncertainty in future GPP predictions when relying on process-based models [15].

Another powerful approach for the evaluation of the impact of climate change on GPP involves the use of machine learning (ML) models. With advancements in remote sensing and ML technologies, the assessment and estimation of GPP using ML models have become a prominent research focus [16–18]. Leveraging their strong non-linear fitting capabilities, ML models are adept in capturing the complex non-linear relationships between GPP and various influencing factors, such as meteorological and soil conditions. For instance, Yao et al. [19] employed a model tree ensemble algorithm to create a GPP dataset over China with a spatial resolution of 0.1°, spanning from 1982 to 2015, using in situ data from 40 flux sites. To further improve the precision of GPP simulations, researchers have also conducted comparative studies on the performance of different ML models [20,21]. For example, Wang et al. [22] compared six ML models—a multilayer perceptron, random forest [23], Adaboost, gradient boosting decision tree, XGBoost, and LightGBM—trained using remote sensing data and various influencing factors. In addition to their accuracy in GPP simulation, ML models contribute to the attribution analysis of GPP variations. For instance, Yao et al. [19] identified the temperature as the dominant climatic driver of the GPP at a national scale. Similarly, Ma et al. [24] showed that the leaf area index and temperature-related factors had the largest relative impacts on the GPP in Northern and Southern China, respectively. This capability is crucial in evaluating the impacts of climate change on GPP. Unlike process-based physical models, which rely on a set of fixed input variables, ML-based models can incorporate a broader range of variables—such as greenness and the land surface temperature—to enhance the GPP simulation accuracy [25].

Despite the substantial advantages of ML models in predicting GPP, research in this field, particularly in the Tibetan Plateau, remains limited. Most current GPP prediction efforts continue to rely on process-based physical models. For instance, Hou et al. [26] employed the CoLM model to examine the effects of changes in land use and land cover on the future terrestrial GPP. Similarly, GCMs have provided valuable insights into GPP

dynamics. Zhang et al. [27] highlighted the potential risks to GPP in the high-latitude regions of the Northern Hemisphere due to climate change, which poses a direct threat to the global land carbon sink. Furthermore, Xu et al. [28], drawing on data from 13 ESMs, underscored the increasing influence of extreme droughts on GPP throughout the twenty-first century. Projections by Yan et al. [29] indicate divergent trends in GPP, with expected increases in the Northern Hemisphere and decreases in tropical regions. The existing studies on ML used to predict GPP are concentrated on global-scale projections. For example, Huang et al. [30] analyzed future global GPP trends using datasets from 18 ESMs in CMIP6, showing an overall increase in GPP across all four SSP scenarios, with the ssp585 scenario stimulating the most substantial growth. Moreover, the study of Lu et al. [31] indicates that the global GPP is predicted to increase under future climate change in the 21st century. Despite these global-scale studies, there is a noticeable research gap regarding the Tibetan Plateau's GPP under future climate scenarios. Considering that climate change significantly impacts the vegetation composition and functionality [32], it is critical to address the spatiotemporal variations in the GPP in the Tibetan Plateau under changing climate conditions. Employing ML models to predict these variations is not only essential but also strategically crucial in addressing effective ecosystem management.

When selecting an ML model for the prediction of GPP, it is essential to recognize that most existing algorithms are not well suited for the automatic learning of spatial structures and hierarchical features within images. These algorithms often overlook the influence of neighboring grid point variables on GPP [22,31]. Over the past few decades, convolutional neural networks (CNNs) have achieved unprecedented success in addressing computer vision challenges due to their ability to extract complex features and learn compact representations [33]. As a leading paradigm in deep learning, the CNN has significant potential in predicting the spatiotemporal variation in the future GPP. However, the application of CNNs in modeling and predicting the GPP in the Tibetan Plateau remains largely unexplored. Therefore, predicting the annual and seasonal GPP dynamics in response to future climate change in the Tibetan Plateau using a CNN model is crucial in deepening our understanding of vegetation–climate interactions.

To address the challenges posed by climate change on GPP in the 21st century, this study employed a data-driven approach to predict both annual and seasonal variations in the GPP in the Tibetan Plateau. Specifically, a CNN model was utilized to establish nonlinear relationships between the GPP and various environmental factors. This study utilized the GPP dataset developed by Wang et al. [34] to represent the historical monthly distribution of the GPP, while climate variables, CO₂ concentrations, and terrain attributes were incorporated as key environmental factors. Additionally, future climate scenarios from the Coupled Model Intercomparison Project Phase 6 (CMIP6), including SSP1–2.6 (ssp126), SSP2–4.5 (ssp245), SSP3–7.0 (ssp370), and SSP5–8.5 (ssp585), were considered to project future GPP changes. The primary objectives of this study were (1) to predict the annual and seasonal GPP up to the year 2100 under different future scenarios using a data-driven approach; (2) to examine the spatiotemporal variations in the future GPP and analyze their implications; and (3) to assess the relative importance of multiple environmental factors in predicting the GPP. This study could enhance the understanding of the complex interactions between vegetation and the climate and provide critical insights for the formulation of effective management practices to enhance the carbon sequestration capabilities and achieve carbon neutrality goals.

2. Study Area and Data

2.1. Study Area

The Tibetan Plateau (Figure 1), referred to as the “Roof of the World”, is a unique and critical research region due to its vast size and diverse environmental conditions. Located in Central Asia, the Tibetan Plateau covers over 2.5×10^6 km² and has average elevation exceeding 4500 m, making it the highest and largest plateau in the world. The region's topography is uneven, with elevation decreasing from west to east, featuring flat

valleys and plains alongside towering mountain ranges [9]. The Tibetan Plateau is rich in frozen soil, snow, and glacial resources, playing a pivotal role in the Asian hydrological cycle. It serves as the source of major rivers, such as the Yangtze, Yellow, and Mekong, earning its designation as the “Water Tower of Asia”. The plateau also supports a wide range of ecosystems with unique flora and fauna that have adapted to its harsh climate, characterized by cold temperatures, strong winds, and fluctuating diurnal temperatures. Moreover, the Tibetan Plateau is extremely sensitive to global climate change. Over the past 50 years, the mean annual temperature on the Tibetan Plateau has increased by 0.3 °C per decade, a rate significantly higher than in other regions of China [35]. This rapid warming has profound effects on the alpine vegetation, including an advanced spring phenology and enhanced plant carbon fixation capacity. The major vegetation types on the Tibetan Plateau include alpine grasslands, alpine meadows, shrubs, and forests [36]. Alpine grasslands dominate the plateau, consisting primarily of hardy grasses and sedges adapted to high altitudes and cold conditions. The GPP is a key focus of study in this region, as it represents the total carbon fixed by photosynthetic organisms, offering critical insights into carbon sequestration and ecosystem productivity.

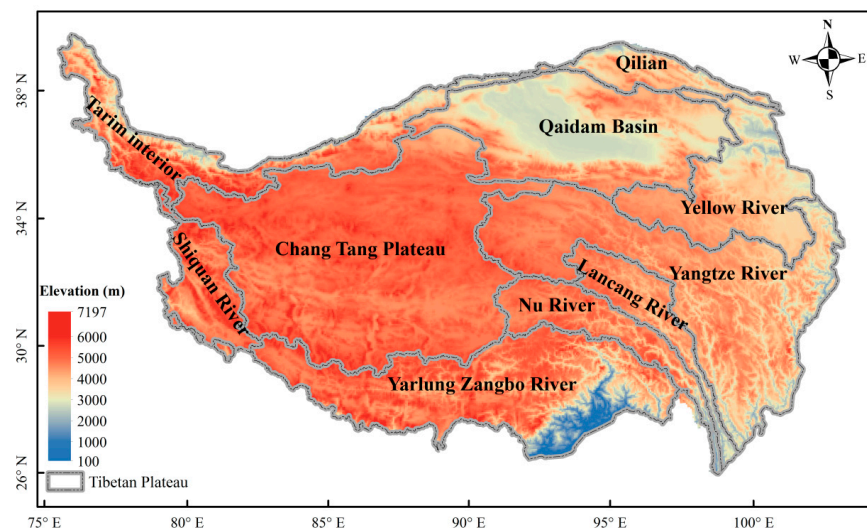


Figure 1. Location of the Tibetan Plateau.

2.2. Data

2.2.1. GPP NIRv Data

The GPP NIRv dataset, developed by Wang et al. [34], marks a significant improvement in estimating GPP using satellite-based near-infrared reflectance (NIRv). Covering the period from 1982 to 2018 with a spatial resolution of 0.05°, this dataset provides extensive long-term data, effectively capturing monthly GPP variations, crucial in understanding global carbon dynamics. The dataset was established through empirical relationships between NIRv and GPP, based on data from 104 eddy covariance flux sites across various climate zones and vegetation types, ensuring its reliability and broad applicability. Validation showed strong correlations between the GPP NIRv and observed GPP, with an R^2 of 0.71 for monthly variations, confirming its effectiveness in tracking temporal GPP changes. Furthermore, comparisons with other global GPP products, such as the FLUXCOM GPP and TRENDY GPP, demonstrated that the GPP NIRv not only aligns closely with these datasets but also offers a more consistent depiction of the long-term GPP trends, especially when compared to process-based models.

The global GPP estimated using NIRv during the study period averaged $128.3 \pm 4.0 \text{ Pg C year}^{-1}$, consistent with other GPP estimates, further highlighting the value of the GPP NIRv dataset in enhancing the understanding of terrestrial carbon fluxes. This dataset is a critical tool for researchers and policymakers, offering a reliable, long-term

resource that supports climate change mitigation efforts and advances the understanding of the global carbon dynamics. This dataset can be downloaded from the TPDC “<https://data.tpd.cn/zh-hans/data/d6dff40f-5dbd-4f2d-ac96-55827ab93cc5> (accessed on 30 September 2024)”. In this study, the GPP NIRv dataset is treated as observational data and utilized as the target GPP in an ML approach to optimize the parameters of the CNN model.

2.2.2. Climate Variables

In this study, the Tibetan Plateau Meteorological Forcing Dataset (TPMFD) was used to train the CNN model for the historical period of 1982–2013. Developed by Jiang et al. [37], the TPMFD integrates high-resolution WRF simulations, long-term ERA5 data [38], and station observations using a deep learning model. Spanning from 1979 to 2020, this dataset offers high-spatial-resolution ($1/30^\circ$) meteorological data for the Tibetan Plateau at monthly, daily, and hourly intervals. Six climate variables—precipitation (prcp), temperature (temp), specific humidity (shum), wind speed (wind), longwave radiation (lard), and shortwave radiation (srad)—were selected for this study as they are critical drivers of plant photosynthesis and ecosystem productivity. These variables directly influence key physiological processes in plants, such as photosynthesis and transpiration, while also playing a significant role in regulating the energy balance within ecosystems. Notably, prcp, temp, and shum are derived from the fusion of short-term WRF simulations with long-term ERA5 data and station observations, providing higher precision compared to conventional reanalysis datasets. The TPMFD is a crucial resource for climate analysis, land surface studies, and ecological modeling in the Third Pole region. The dataset is publicly available at <https://data.tpd.cn/zh-hans/data/44a449ce-e660-44c3-bbf2-31ef7d716ec7> (accessed on 30 September 2024).

In this study, climate variables from the NEX-GDDP-CMIP6 dataset were used to predict the future GPP under four SSP scenarios: ssp126, ssp245, ssp370, and ssp585 [39,40]. These scenarios represent different socioeconomic pathways, ranging from sustainable development (ssp126) and middle-of-the-road growth (ssp245) to uneven regional development (ssp370) and fossil-fuel-intensive futures (ssp585) [30]. The NEX-GDDP-CMIP6 dataset provides downscaled climate projections at a $0.5^\circ \times 0.5^\circ$ spatial resolution, offering detailed insights into future environmental changes [39]. This study used projected data from 2021 to 2100, derived from seven ESMs under these SSP scenarios, as outlined in Table 1, which can be downloaded from <https://nex-gddp-cmip6.s3.us-west-2.amazonaws.com/index.html#NEX-GDDP-CMIP6/> (accessed on 30 September 2024). The climate variables selected—precipitation (prcp), temperature (temp), specific humidity (shum), wind speed (wind), longwave radiation (lard), and shortwave radiation (srad)—are critical in understanding vegetation growth and GPP dynamics, influencing spatial and temporal variations in primary productivity [14]. These variables were therefore chosen to forecast the future GPP.

Table 1. Brief introduction to the employed GCMs from NEX-GDDP-CMIP6.

GCM Model	Spatial Resolution	Research Institute and Country
ACCESS-CM2	$0.25^\circ \times 0.25^\circ$	Commonwealth Scientific and Industrial Research Organization (CSIRO) and the Bureau of Meteorology (BoM), Australia
CanESM5	$0.25^\circ \times 0.25^\circ$	Canadian Centre for Climate Modelling and Analysis (CCCma), Canada
CNRM-CM6-1	$0.25^\circ \times 0.25^\circ$	Centre National de Recherches Météorologiques (CNRM), France
MIROC6	$0.25^\circ \times 0.25^\circ$	Japan Agency for Marine-Earth Science and Technology (JAMSTEC), Japan
BCC-CSM2-MR	$0.25^\circ \times 0.25^\circ$	Beijing Climate Center, China Meteorological Administration, Beijing, China
MPI-ESM1-2-LR	$0.25^\circ \times 0.25^\circ$	Max Planck Institute for Meteorology (MPI-M), Germany
UKESM1-0-LL	$0.25^\circ \times 0.25^\circ$	A collaborative effort between the Met Office Hadley Centre and the Natural Environment Research Council (NERC), United Kingdom

2.2.3. CO₂ Concentration and Terrain Attributes Data

For GPP prediction, this study used global monthly gridded atmospheric CO₂ concentration data, which are crucial in evaluating the impact of CO₂ fertilization on terrestrial ecosystems [41]. The dataset provides CO₂ concentration values at a 1° spatial resolution, covering both historical (1982–2013) and future (2021–2100) periods across four SSP scenarios [42]. It captures spatial, seasonal, and annual variations in CO₂ levels, offering a detailed representation of the atmospheric CO₂ distribution—critical for accurate GPP forecasts. Additionally, the Global Multi-Resolution Terrain Elevation Data 2010, initially at a 30 arc-second resolution, were resampled to 0.05° using bilinear interpolation. Five terrain attributes—elevation, slope, aspect, latitude, and longitude—were incorporated into the CNN model for simulation and projection [43].

3. Methodology

3.1. Convolutional Neural Networks

CNNs are a powerful class of deep learning models specifically designed for the analysis of visual data. The core of the CNN lies in its use of convolutional layers, which automatically and adaptively learn the spatial hierarchies of features from raw input data [33]. A typical CNN architecture includes convolutional layers, pooling layers, and fully connected layers. Convolutional layers use filters or kernels to slide over the input data, extracting local patterns or features. Pooling layers then reduce the spatial dimensions of these feature maps, lowering the computational complexity while retaining key information. Finally, fully connected layers synthesize the learned features to perform tasks like classification or regression. One of the CNNs' key strengths is their ability to learn hierarchical representations of the features directly from raw data, enabling them to capture complex patterns and dependencies within images. This makes CNNs highly effective for tasks such as object detection, image segmentation, and facial recognition.

The CNN used in this study (Figure 2) consists of a sequence of layers designed for effective feature extraction and robust training. It begins with a 2D convolutional layer with a fixed 3×3 kernel size and 32 filters, followed by a max-pooling layer with a 2×2 pool size. This pattern is repeated with a second 2D convolutional layer, this time with 64 filters, followed by another max-pooling layer. A flattened layer is then added to convert the 2D spatial data into a 1D vector, preparing them for the dense layers. The model includes a fully connected dense layer with 128 neurons, followed by a Monte Carlo dropout layer with a 50% dropout rate to mitigate overfitting. The final dense layer, optimized for the task, leads to a single output neuron using a linear activation function, suitable for regression tasks.

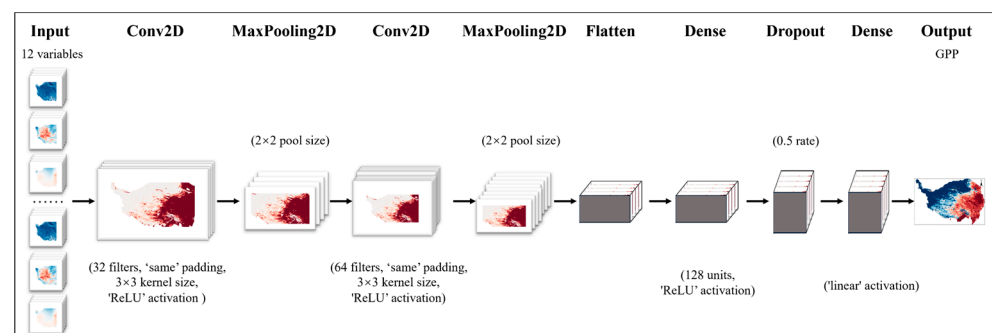


Figure 2. Scheme of the CNN model used for the GPP forecasts.

The model was trained using the Adam optimizer over a maximum of 1000 epochs, with an initial learning rate of 0.001. Gradient clipping was applied to prevent exploding gradients, and early stopping with a patience of 150 epochs was employed to further reduce overfitting. The activation function for the output layer was “linear”, while “ReLU” was applied to the other layers. The loss function used was the “mean squared error”. Hyperparameters, including a batch size of 32 and “same” padding, were optimized using

Bayesian methods. The model was implemented in Python 3.7.13 using TensorFlow and the Keras API. All data were resampled to a 0.05° resolution using bilinear interpolation to match the spatial resolution of the GPP NIRv data. To avoid the risk of overestimating the model's performance [44], the monthly data from the historical period of 1982 to 2013 were segmented, with the period from 1982 to 2007 designated for training and the subsequent period from 2007 to 2013 for testing. During the prediction period, the results for each scenario represent the arithmetic mean of the seven ESMs. This study employs the bootstrap method to estimate the 95% confidence intervals for the predictions under each scenario. The bootstrap is a statistical technique that repeatedly samples with replacement from the original dataset to estimate the distribution of a statistic, allowing for the calculation of confidence intervals.

To determine the relative importance of the input variables in a CNN model using feature importance scoring (i.e., permutation importance), the following steps are taken. Train the CNN on a dataset to learn the relationship between the input features and output targets. Then, evaluate the model on a test or validation set to establish the baseline performance. For each input variable, shuffle its values while keeping the others intact and re-evaluate the model's performance. The importance score is calculated by measuring the performance drop due to shuffling; a larger performance drop indicates higher importance. Repeat this process for all input variables, rank them according to their importance scores, and interpret the results accordingly. This approach provides a clear understanding of the relative importance of each variable in the CNN's predictions.

3.2. Performance Measures

The following four commonly used and easily understood performance measures were used to qualitatively evaluate the performance of the ML models: root mean squared error (RMSE), coefficient of determination (R^2), *PBIAS*, and *MAE*. Their detailed expressions are as follows:

$$RMSE = \sqrt{\frac{\sum_{i=1}^n (y_{sim} - y_{obs})^2}{n}} \quad (1)$$

$$R^2 = 1 - \frac{\sum_{i=1}^n (y_{obs} - y_{sim})^2}{\sum_{i=1}^n (y_{obs} - \bar{y}_{obs})^2} \quad (2)$$

$$PBIAS = \frac{\sum_{i=1}^n (y_{sim} - y_{obs})}{\sum_{i=1}^n y_{obs}} \times 100 \quad (3)$$

$$MAE = \frac{1}{n} \sum_{i=1}^n |y_{sim} - y_{obs}| \quad (4)$$

where n is the number of observations; y_{sim} represents the simulated GPP; y_{obs} is the target GPP; and \bar{y}_{obs} denotes the average of the target GPP. The R^2 ranges from 0 to 1. A value of 0 indicates that the model does not explain any variability in the dependent variable, whereas a value of 1 indicates that the model explains all of the variability. The *RMSE* measures the standard deviation of the differences between the predicted and target variables. Lower *RMSE* values are preferable, signifying closer agreement between the predictions and targets. A *PBIAS* value of 0% indicates a perfect model fit with no bias. Positive values indicate that the model predictions are, on average, higher than the observed values (overestimation) and vice versa. The *MAE* provides a straightforward measure of the prediction accuracy, with lower values indicating better model performance.

4. Results

4.1. Performance of GPP Simulation

Figure 3 depicts the variation in the loss function over the epochs. The model shows signs of stabilization after approximately 800 iterations. Table 2 summarizes the accuracy of the GPP simulations, with R^2 values of 0.994 for the training period and 0.978 for the testing period. The corresponding *RMSE* values are 0.075 and 0.127, respectively. Additionally, a

comparison of other metrics, such as the *MAE* and *PBIAS*, between the two periods further underscores the strong generalization capability of the CNN model. Overall, the R^2 , *RMSE*, *MAE*, and *PBIAS* for the entire period are 0.988, 0.093, 0.070, and 0.577%, respectively, demonstrating that the CNN model could simulate the GPP effectively.

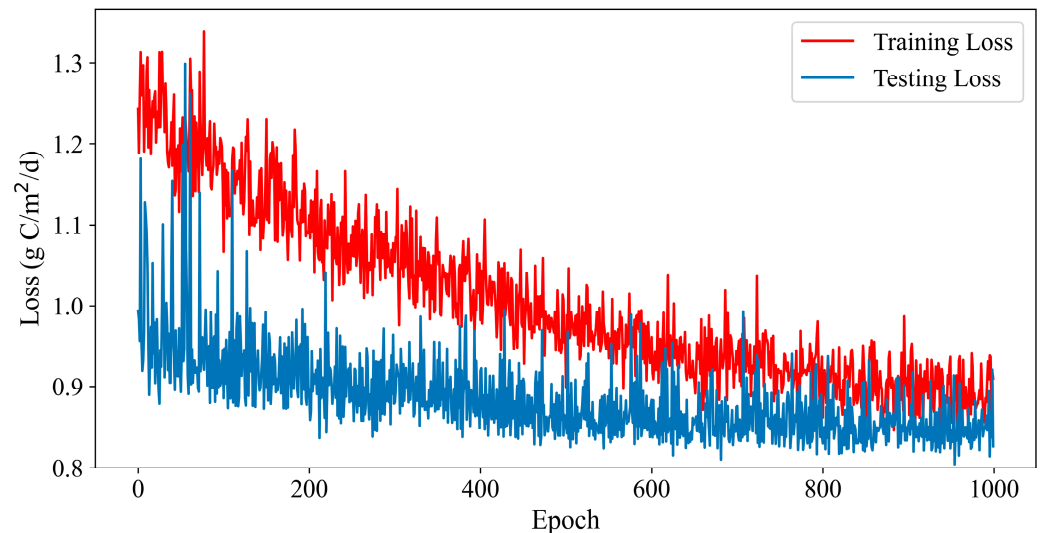


Figure 3. Summarized results of loss for CNN model on training and testing datasets.

Table 2. Assessment of historical simulation accuracy for seasonal and annual GPP.

Evaluation Criterion	Training	Testing	All	Spring	Summer	Autumn	Winter
R^2	0.994	0.968	0.978	0.799	0.863	0.762	0.778
<i>RMSE</i>	0.075	0.127	0.093	0.041	0.064	0.071	0.052
<i>MAE</i>	0.061	0.091	0.070	0.036	0.046	0.051	0.049
<i>PBIAS</i>	2.077%	−1.786%	0.577%	5.342%	−0.663%	−4.537%	9.182%

Note: the unit of the *RMSE* and *MAE* is $\text{g C}\cdot\text{m}^{-2}\cdot\text{d}^{-1}$.

From a seasonal perspective, the model performs best in simulating the summer GPP, followed by autumn and then spring, with winter showing the lowest accuracy. Notably, the model tends to overestimate the GPP during winter and spring, while underestimating it in summer and autumn. This pattern suggests that the CNN model struggles in capturing extreme GPP values, leading to the overestimation of lower values and the underestimation of higher values.

The coefficient of determination R^2 between the simulated and observed GPP in the testing period, as depicted in Figure 4, was used to assess the spatial performance of the CNN model. The spatial distribution of the R^2 shows a gradual decrease from east to west, with higher values concentrated in the Qilian Mountains and the basins of the Yellow, Yangtze, Lancang, and Yarlung Zangbo Rivers. In the Qilian Mountains and the Yellow, Yangtze, and Lancang River Basins, the R^2 values generally range from 0.7 to 0.9, with some low-altitude areas exceeding 0.9, indicating a strong correlation between the simulated and observed GPP. In contrast, the R^2 values in the Yarlung Zangbo River Basin range from 0.5 to 0.7, reflecting slightly lower accuracy in this region. In other areas, the R^2 values range between 0 and 0.3, likely due to lower GPP levels, which introduce greater uncertainty into the simulation. Despite these regional variations, the overall performance of the CNN model remains robust, underscoring its potential as a valuable tool for the prediction of GPP on the Tibetan Plateau under future climate scenarios.

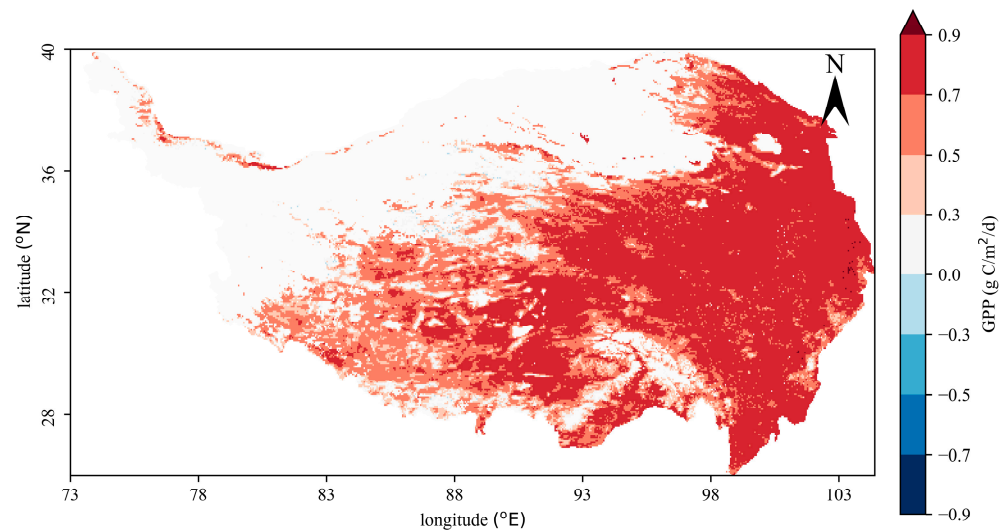


Figure 4. Spatial patterns of R^2 between monthly simulated GPP and observed GPP in the testing period.

4.2. Temporal Variation in GPP

Figure 5 illustrates the historical changes in the annual GPP and the projected future changes under four SSP scenarios on the Tibetan Plateau. It indicates a significant increasing trend in the annual GPP during the historical period, which continues, albeit at a more gradual pace. Moreover, the rate of increase is projected to escalate as the forcing levels intensify in future scenarios. Statistical analysis (Table 3) reveals that, between 1982 and 2018, the average annual GPP on the Tibetan Plateau was $363.80 \text{ g C}\cdot\text{m}^{-2}\cdot\text{year}^{-1}$, with a growth rate of $1.033 \text{ g C}\cdot\text{m}^{-2}\cdot\text{year}^{-1}$. In the period from 2021 to 2060, the projected average annual GPP under the ssp126, ssp245, ssp370, and ssp585 scenarios is $384.908 \text{ g C}\cdot\text{m}^{-2}\cdot\text{year}^{-1}$, $385.319 \text{ g C}\cdot\text{m}^{-2}\cdot\text{year}^{-1}$, $385.493 \text{ g C}\cdot\text{m}^{-2}\cdot\text{year}^{-1}$, and $386.368 \text{ g C}\cdot\text{m}^{-2}\cdot\text{year}^{-1}$, respectively. Compared to the baseline period of 1982–2018, the growth rates are 5.74%, 5.85%, 5.90%, and 6.15%. By the period from 2061 to 2100, these average values are expected to increase to $388.321 \text{ g C}\cdot\text{m}^{-2}\cdot\text{year}^{-1}$, $394.338 \text{ g C}\cdot\text{m}^{-2}\cdot\text{year}^{-1}$, $398.535 \text{ g C}\cdot\text{m}^{-2}\cdot\text{year}^{-1}$, and $401.293 \text{ g C}\cdot\text{m}^{-2}\cdot\text{year}^{-1}$, resulting in growth rates of 6.68%, 8.33%, 9.48%, and 10.24% relative to the 1982–2018 baseline.

Table 3. The trends and p -values for the annual GPP changes in the historical and projected future periods during the 21st century under the ssp126, ssp245, ssp370, and ssp585 scenarios.

	Historical 1982–2018	ssp126 2021–2060	ssp126 2061–2100	ssp245 2021–2060	ssp245 2061–2100	ssp370 2021–2060	ssp370 2061–2100	ssp585 2021–2060	ssp585 2061–2100
trend	1.033	0.199	0.155	0.299	0.258	0.355	0.375	0.401	0.325
p	<0.01	<0.01	<0.01	<0.01	<0.01	<0.01	<0.01	<0.01	<0.01

Note: the unit of the trend is $\text{g C}\cdot\text{m}^{-2}\cdot\text{year}^{-1}$; if the p -value is less than 0.01, the value of p is marked as <0.01.

Furthermore, the rates of change in the annual GPP for the periods 2021–2060 and 2061–2100 were analyzed. Under the ssp126 scenario, the growth rates for these periods are $0.199 \text{ g C}\cdot\text{m}^{-2}\cdot\text{year}^{-1}$ and $0.155 \text{ g C}\cdot\text{m}^{-2}\cdot\text{year}^{-1}$, respectively. The p -values for trend significance in both periods are less than 0.01, indicating that the changes in GPP under this scenario are statistically significant. Additionally, the trend and corresponding p -value for the overall period 2021–2100 under the SSP126 scenario are $0.108 \text{ g C}\cdot\text{m}^{-2}\cdot\text{year}^{-1}$ and 4.470×10^{-7} , respectively. This suggests that the slight increase in GPP projected by 2100 compared to 2021 is likely within the range of normal variability. In contrast, the ssp245 scenario shows a more pronounced growth rate of $0.299 \text{ g C}\cdot\text{m}^{-2}\cdot\text{year}^{-1}$ from 2021 to 2060, which slightly increases to $0.258 \text{ g C}\cdot\text{m}^{-2}\cdot\text{year}^{-1}$ for the period of 2061–2100. Notably, the ssp370 and ssp585 scenarios exhibit more substantial increases in GPP. Under the

ssp370 scenario, the annual GPP growth rate is $0.355 \text{ g C} \cdot \text{m}^{-2} \cdot \text{year}^{-1}$ before 2060, rising to $0.375 \text{ g C} \cdot \text{m}^{-2} \cdot \text{year}^{-1}$ from 2061 to 2100. These findings highlight the varying impacts of different socioeconomic pathways on the GPP, with more aggressive scenarios resulting in greater changes in GPP over time.

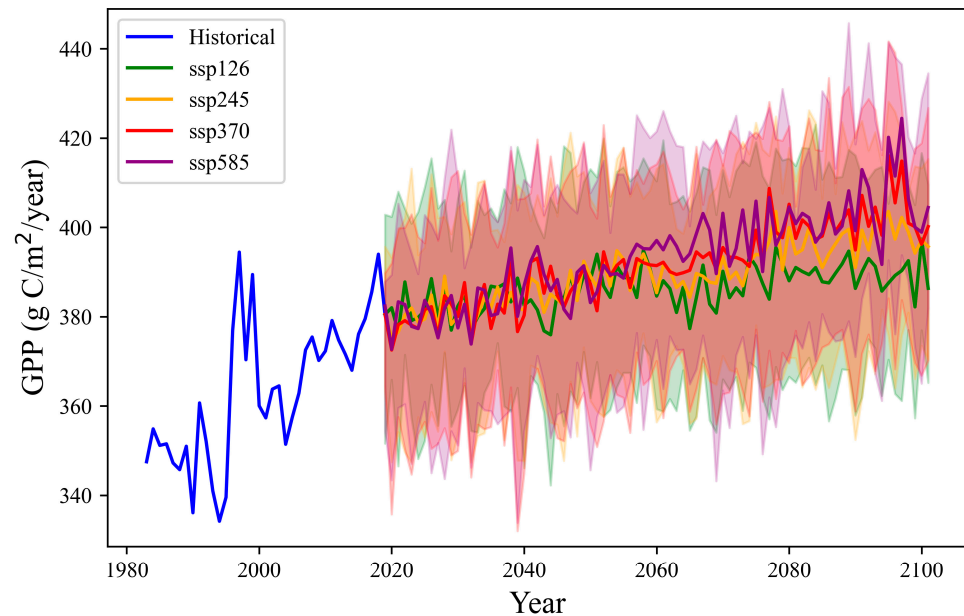


Figure 5. The historical changes in the annual GPP (blue line) and the projected future changes during the 21st century under the ssp126 (green line), ssp245 (yellow line), ssp370 (red line), and ssp585 (purple line) scenarios on the Tibetan Plateau. The shaded regions depict the 95% confidence intervals for the predicted GPP during the future period.

In the ssp585 scenario, characterized by fossil-fuel-driven development, the GPP growth rate is projected to be $0.401 \text{ g C} \cdot \text{m}^{-2} \cdot \text{year}^{-1}$ from 2021 to 2060, followed by a significant decline to $0.325 \text{ g C} \cdot \text{m}^{-2} \cdot \text{year}^{-1}$ after 2060. These findings suggest that scenarios with lower forcing levels, such as ssp126 and ssp245, exhibit lower GPP growth rates after 2060 compared to the preceding period. Conversely, scenarios with higher forcing levels, such as ssp370, indicate an increase in the GPP growth rates after 2060, with the exception of ssp585. This phenomenon suggests that higher temperatures and levels of CO_2 emissions, coupled with more frequent extreme weather events such as droughts, could have adverse effects on plant growth [28]. Although ssp370 also involves elevated CO_2 emissions, the temperatures in high-altitude regions may not yet reach the critical thresholds that inhibit plant growth. In contrast, under ssp585, higher temperatures are likely to negatively impact plant growth. In short, the annual GPP is expected to significantly increase throughout the 21st century under all future climate scenarios.

The statistical analysis reveals that, between 2021 and 2100, the average uncertainty interval for the annual GPP on the Tibetan Plateau is $21.301 \text{ g C} \cdot \text{m}^{-2} \cdot \text{year}^{-1}$, $30.428 \text{ g C} \cdot \text{m}^{-2} \cdot \text{year}^{-1}$, $22.326 \text{ g C} \cdot \text{m}^{-2} \cdot \text{year}^{-1}$, and $24.684 \text{ g C} \cdot \text{m}^{-2} \cdot \text{year}^{-1}$ under the ssp126, ssp245, ssp370, and ssp585 scenarios, respectively. Overall, the uncertainty interval will increase with the increase in CO_2 emissions, and the uncertainty interval in the ssp245 scenario is significantly larger.

Figure 6 illustrates both the historical seasonal GPP from 1982 to 2018 and the projected seasonal GPP from 2021 to 2100 under the four SSP scenarios. The data reveal pronounced seasonal patterns in the GPP. The GPP shows the most significant increase in summer, while there is essentially no change in winter, and it even gradually decreases. This seasonal variation is primarily attributed to the synchronized occurrence of precipitation and warmth in the region, which provides favorable conditions for vegetation growth and development during summertime. The adequate temperature and moisture levels

during this season improved the biomass compared to other seasons. In contrast, only vegetation at lower altitudes continues to grow during the winter months, while plants in higher-altitude regions show halted growth or undergo seasonal senescence due to the cold temperatures.

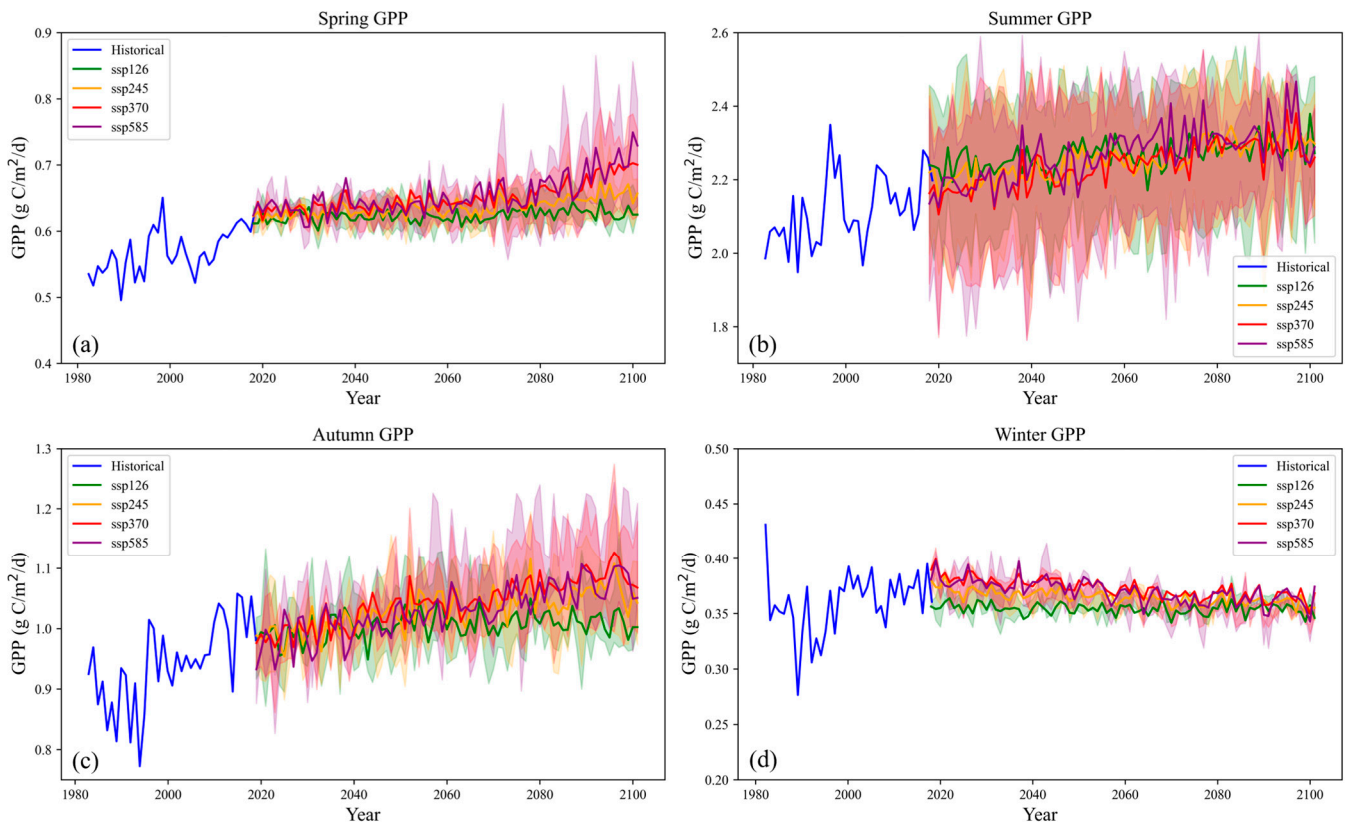


Figure 6. The seasonal GPP dynamics during the historical (blue line) and 2021–2100 periods under the ssp126 (green line), ssp245 (yellow line), ssp370 (red line), and ssp585 (purple line) scenarios. The shaded regions depict the 95% confidence intervals for the predicted GPP during the future period.

During the historical period, the GPP showed an increasing trend, with the spring, summer, and autumn GPP trends passing the 99% significance test. However, the winter GPP trend did not pass the 99% significance test (Table 4). This can be attributed to the cold winter temperatures, weak solar radiation, and decreased precipitation in the form of snow, which leads to soil freezing on the Tibetan Plateau. As a result, vegetation growth is largely suspended, with most plants either showed paused growth or dying back during winter, leading to the lowest GPP values of the year. Although the temperature has increased, it remains insufficient to stimulate plant growth on the Tibetan Plateau, which does not result in a noticeable trend in the GPP during winter.

The GPP in both spring and autumn showed a significant upward trend under the ssp245, ssp370, and ssp585 scenarios, particularly in spring, where the trend passed the 99% significance test for the period of 2061–2100. This trend is primarily driven by gradually rising temperatures, especially in high-altitude and cold regions like the Tibetan Plateau, which promote earlier vegetation growth and enhance photosynthesis. In autumn, the delayed occurrence of phenological events, particularly the postponement of plant senescence, extends the growing season and contributes to increased GPP. Moreover, rising atmospheric CO₂ concentrations further stimulate photosynthesis, particularly at the beginning of the growing season, leading to increases in GPP during both spring and autumn.

Table 4. The trends and *p*-values for the seasonal GPP changes in the historical and projected future periods during the 21st century under the ssp126, ssp245, ssp370, and ssp585 scenarios.

Seasonal		Historical	ssp126		ssp245		ssp370		ssp585	
		1982–2018	2021–2060	2061–2100	2021–2060	2061–2100	2021–2060	2061–2100	2021–2060	2061–2100
Spring	trend	1.900	−0.102	0.211	0.249	0.697	0.324	1.501	0.297	1.891
	<i>p</i>	<0.01	0.379	0.088	0.038	<0.01	0.032	<0.01	0.167	<0.01
Summer	trend	4.199	1.228	1.327	1.677	2.159	1.994	1.187	2.984	0.329
	<i>p</i>	<0.01	0.011	<0.01	<0.01	<0.01	<0.01	0.061	<0.01	0.682
Autumn	trend	4.151	0.999	0.072	1.530	0.779	1.820	1.576	1.580	1.493
	<i>p</i>	<0.01	0.012	0.752	<0.01	0.018	<0.01	<0.01	<0.01	<0.01
Winter	trend	0.778	−0.059	0.029	−0.014	−0.153	−0.251	−0.177	−0.250	−0.056
	<i>p</i>	0.074	0.339	0.684	0.017	0.028	<0.01	0.040	<0.01	0.533

Note: the unit of the trend is $10^{-3} \text{ g C} \cdot \text{m}^{-2} \cdot \text{d}^{-1}$. If the *p*-value is less than 0.01, the value of *p* is marked as <0.01; otherwise, the true *p* value is given in the table.

Under the ssp126 scenario, the seasonal GPP fluctuations are minimal. The GPP trends in all seasons fail to pass the 99% significance test, indicating that significant changes in GPP are unlikely under this scenario. In contrast, the ssp245 scenario shows a significant increase in the summer GPP, which passes the 99% significance test. This suggests that, under moderate emission levels, the summer GPP may benefit from the warmer temperatures and improved CO₂ concentrations. Under the ssp370 scenario, spring exhibits accelerated increases in GPP, with both the spring and autumn trends passing the 99% significance test in 2061–2100. This indicates the more robust response of vegetation growth to increased CO₂ levels and warming, particularly in these seasons. The ssp585 scenario presents the most pronounced seasonal variations in the GPP among all scenarios. Spring, summer, and autumn all show accelerated increases in GPP, with significant trends passing the 99% significance test in various time intervals. This scenario, characterized by high greenhouse gas emissions, suggests that vegetation growth on the Tibetan Plateau will be profoundly affected by this climatic scenario, inducing considerable seasonal shifts in the GPP.

4.3. Spatial Variations in GPP

Figure 7 shows the spatial patterns of the annual GPP on the Tibetan Plateau averaged from 1982 to 2018. As shown in the figure, in general, the mean annual GPP decreases gradually from the southeast to the northwest. The regions with higher GPP are primarily distributed in the upper reaches of the Yellow River, Yangtze River, Lancang River, Nu River, and Yarlung Zangbo River. These areas are low in elevation and receive relatively abundant precipitation, which supports the growth of shrubs and grasses. In contrast, areas such as the Chang Tang Plateau, Qaidam Basin, Shiquan River, Tarim Basin, and Qilian Mountains show lower GPP due to their higher elevations, lower temperatures, and limited precipitation, which restrict vegetation growth. According to the statistical results, the mean annual GPP on the Tibetan Plateau was $363.80 \text{ g C} \cdot \text{m}^{-2} \cdot \text{year}^{-1}$. This finding is consistent with the results of You et al. [45].

To illustrate the changes in GPP over different periods, Figure 8 presents the decadal average GPP for 2021–2040, 2041–2060, 2061–2080, and 2081–2100 under the four SSP scenarios as a function of elevation. As seen in Figures 5 and 6, the GPP shows an increasing trend at both the interannual and seasonal scales in future periods. Here, we aim to demonstrate how these changes manifest across different elevations. From Figure 8, it is evident that, under the ssp126 scenario, the overall changes in GPP across different periods are not particularly pronounced, with noticeable relative changes occurring in the 1000–2000 m range, albeit with a limited magnitude. Under the ssp245 scenario, significant differences in GPP can be observed between elevations of 3000 and 4500 m, indicating that, with further temperature increases and CO₂ emissions, vegetation at these elevations is notably affected.

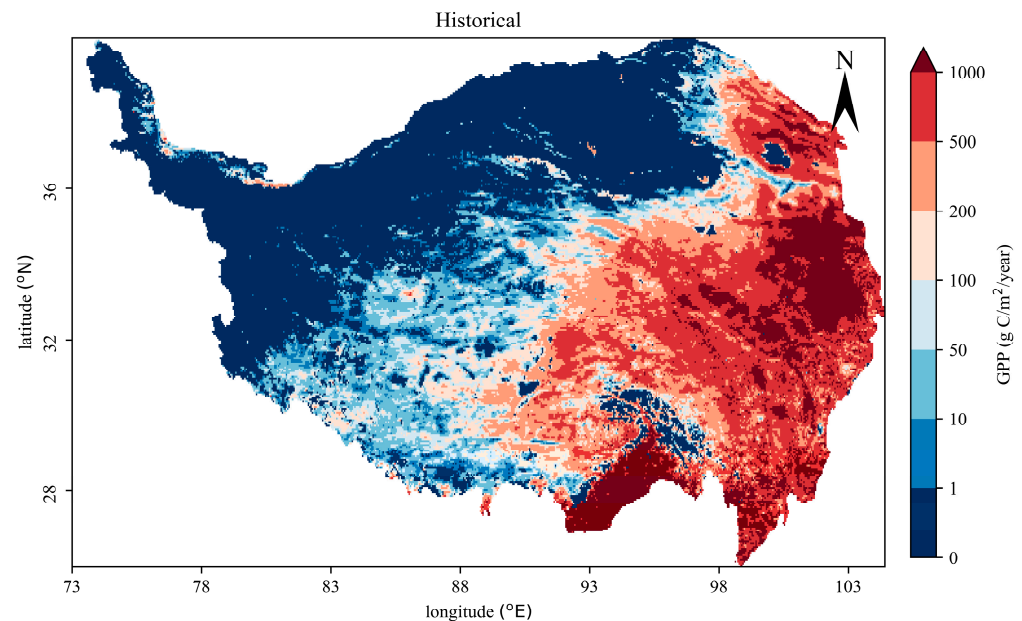


Figure 7. Spatial patterns of annual GPP averaged from 1982 to 2018 on the Tibetan Plateau.

In the ssp370 scenario, the elevation band between 3000 and 4500 m exhibits noticeable changes in GPP across different periods, particularly between 2081 and 2100, which is markedly higher than that in 2061–2080. However, it can also be observed that the GPP during 2041–2060 closely aligns with that of 2021–2040, suggesting a gradual increase in the impact of the temperature and CO₂ on the GPP. Besides the 3000–4500 m range, changes are also noticeable in the 1000–1500 m elevation band.

Under the ssp585 scenario, the range of elevation bands showing significant differences across the periods is broader. In addition to the 3000–4500 m elevation band, significant changes could be observed in the 1000–1500 m range. Although the GPP during 2041–2060 closely aligns with that of 2021–2040, under this scenario, the differences between 2061–2080 and 2041–2060 are substantially greater than those under the other three scenarios. This indicates a stronger GPP response under high-emission scenarios. However, high-emission scenarios may also have negative impacts. The differences between 2081–2100 and 2061–2080 under this scenario are smaller than those under the ssp370 scenario, suggesting that high-emission scenarios do not always favor vegetation growth.

Furthermore, Sen's slope for the annual GPP during the period of 1982–2018 has been computed and is presented in Figure 9 to illustrate the spatial distribution of the GPP trends on the Tibetan Plateau. Sen's slope is used to determine the change rate for time series data [46]. The results reveal substantial spatial heterogeneity in the GPP trends across the region, which is largely attributed to variations in the climatic conditions. Over the past four decades, regions where the GPP changes passed the significance tests are predominantly located in the southeastern part of the plateau. The number of significant grid points gradually decreases from the southeast to the northwest. Notably, areas exhibiting an increasing GPP trend with statistical significance are mainly found in the Yellow River Basin and the Eastern Qilian Mountains. Conversely, regions showing a decreasing GPP trend with statistical significance are primarily located in the middle and upper reaches of the Yarlung Zangbo River, the upper Nu River, and the Qiangtang region. Overall, the Northeastern Tibetan Plateau shows an increasing GPP trend in the next few decades, whereas the GPP is decreasing along the Himalayas from the southeast to the northwest.

When considered alongside Figure 7, it becomes apparent that the significant trends coincide with the spatial distribution of the GPP. Specifically, areas with higher GPP also exhibit pronounced and positive trends, indicating that productive vegetation on the Tibetan Plateau has been more responsive to climate change over the past forty years. Statistically, 43.59% of the area experienced an increasing GPP trend, while 22.31% showed a decreasing

trend. The remaining regions exhibited no significant change. Among these, areas with a significant increasing trend account for 16.02% of the total area of the Tibetan Plateau, whereas those with a significant decreasing trend make up 3.71%. This suggests that the overall trend on the Tibetan Plateau over the last four decades has been predominantly an increase in GPP, aligning with the conclusions drawn in Section 4.2.

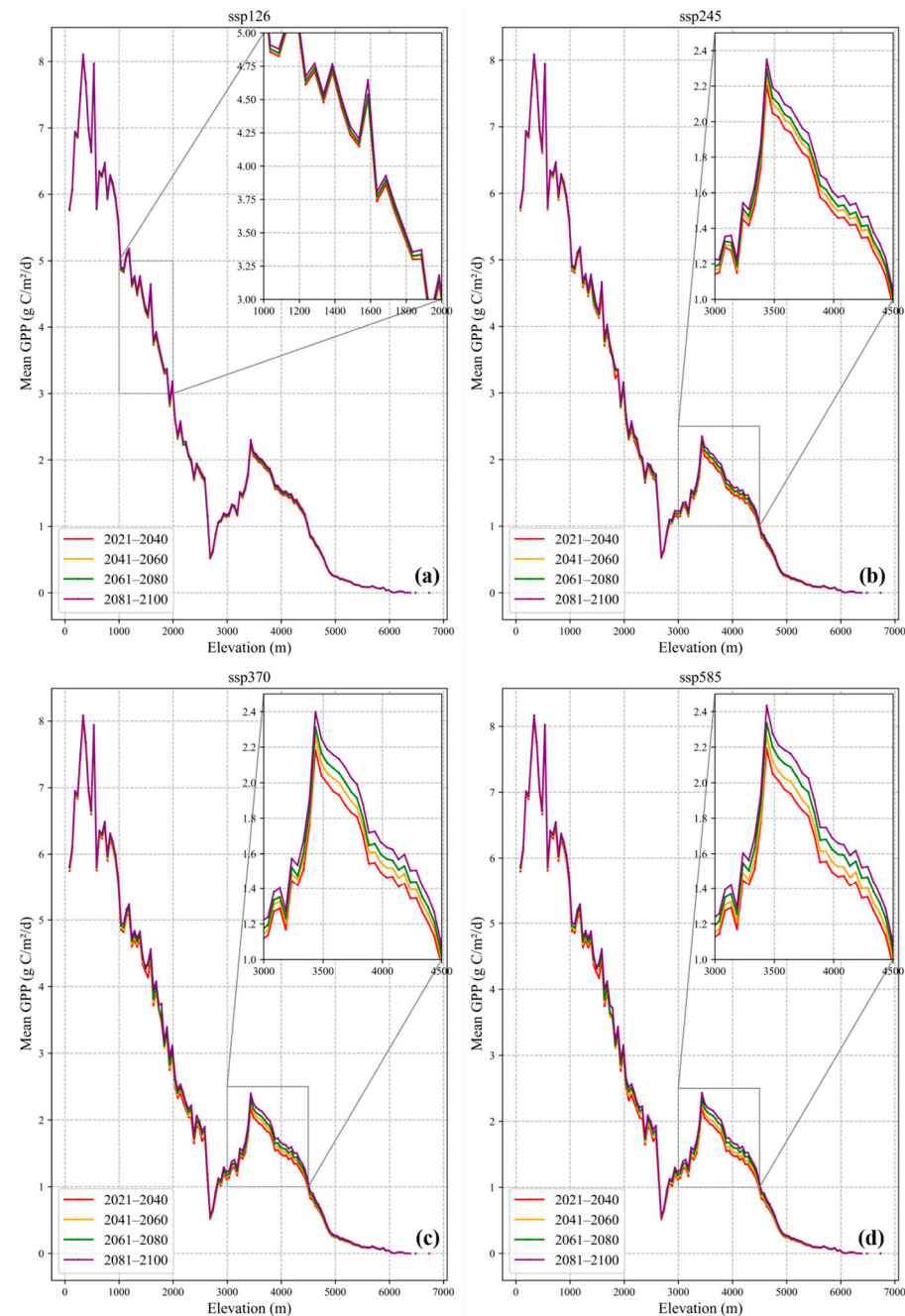


Figure 8. Average of the predicted future GPP per two decades, varying with elevation, on the Tibetan Plateau during 2021–2100 under the (a) ssp126, (b) ssp245, (c) ssp370, and (d) ssp585 scenarios.

Figure 10 illustrates the GPP trends over the 80 years from 2021 to 2100. Similar to Figure 9, only grid points where the changes passed the statistical significance tests are displayed. Under the ssp126 scenario, the majority of the Tibetan Plateau shows no statistically significant trend in the GPP. The statistical analysis reveals that only 55.39% of the grid points show significant changes, with 49.52% exhibiting an increasing trend and 5.87% showing a decreasing trend. This finding is consistent with the conclusions of Section 4.2,

indicating that the GPP on the Tibetan Plateau follows a pattern of normal fluctuation without significant trends. In contrast, under the ssp245 scenario, the number of grid points showing significant changes increases markedly. It is estimated that approximately 86.58% of the Tibetan Plateau displays significant trends, with 73.17% of the grid points showing an increasing trend and 13.41% showing a decreasing trend. The grid points with statistically significant increasing trends are predominantly located in regions with highly productive vegetation, including the Qilian Mountains, Yellow River, Yangtze River, Lancang River, and Yarlung Zangbo River areas.

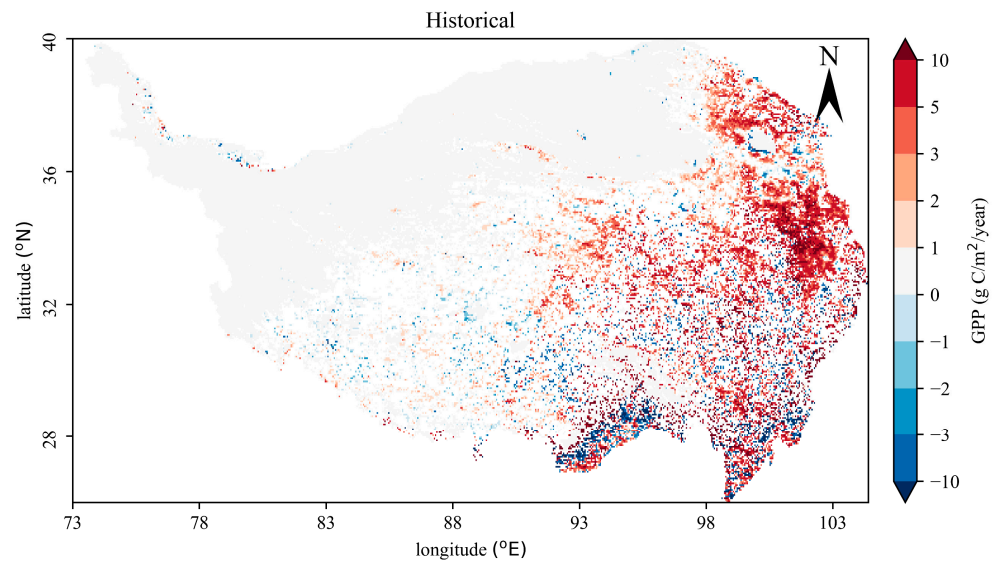


Figure 9. Spatial distribution of trends for annual GPP on the Tibetan Plateau from 1982 to 2018.

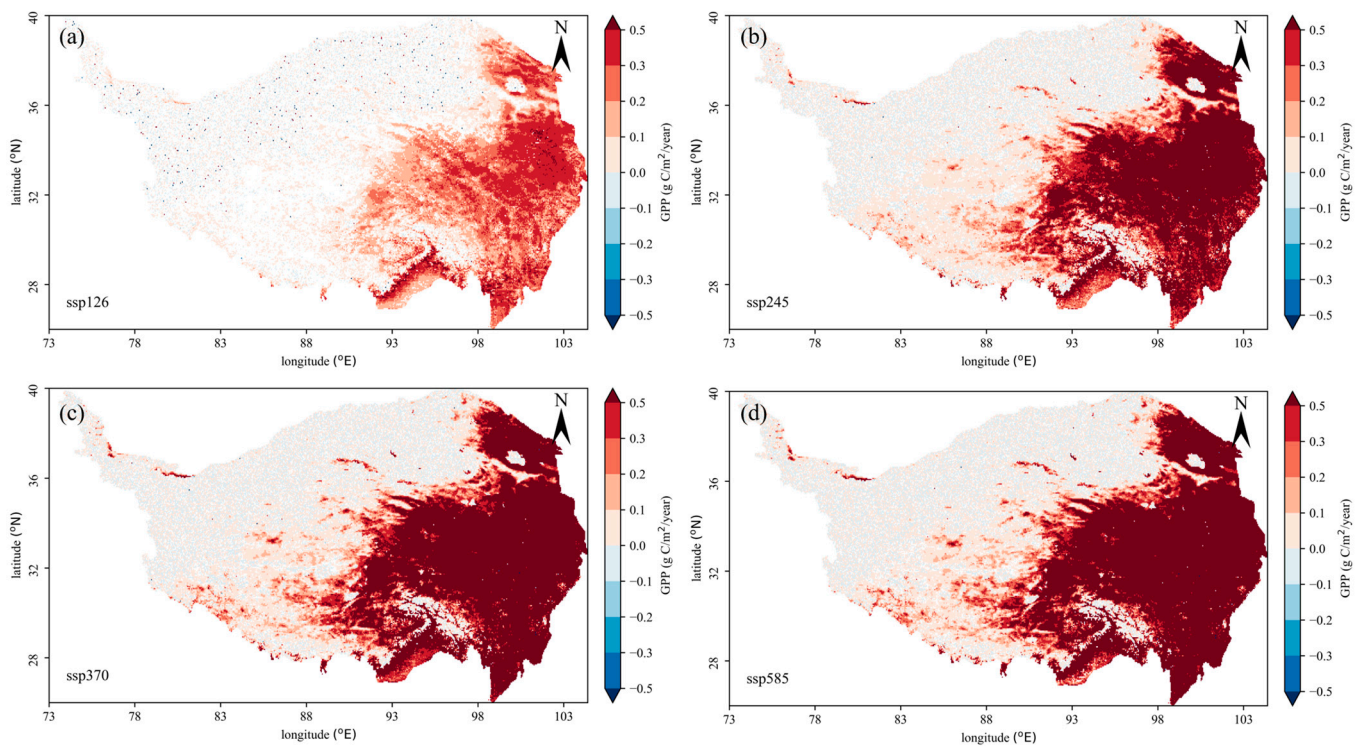


Figure 10. Spatial distribution of trends for annual GPP on the Tibetan Plateau during 2021–2100 under the (a) ssp126, (b) ssp245, (c) ssp370, and (d) ssp585 scenarios.

The spatial distribution patterns under the ssp370 and ssp585 scenarios are largely consistent with those of ssp245. However, the proportion of grid points with statistically significant GPP trends continues to rise, reaching 88.94% under ssp370 and 91.04% under ssp585. Notably, the proportion of points exhibiting a statistically significant increasing trend is 74.16% for ssp370 and 75.87% for ssp585. In summary, the Tibetan Plateau is projected to experience an overall increase in vegetation productivity with localized decreases. There are significant differences in the change characteristics of vegetation productivity across different sub-regions, reflecting the complex interplay of climatic and environmental factors influencing the vegetation dynamics. From the Sen slope of the annual GPP, it can be observed that the increase in the annual GPP in future decades is mainly concentrated in regions with relatively high GPP, such as the northern regions of the Tibetan Plateau, the Yellow River Basin, and the Eastern Qilian Mountains.

5. Discussion

5.1. Relative Importance of Environmental Factors

Figure 11 highlights the relative importance of key environmental factors in the GPP prediction model on the Tibetan Plateau. Among these, longwave radiation (lrad), shortwave radiation (srad), the specific humidity (shum), and speed (wind) are identified as the five most influential factors. Longwave radiation, in particular, stands out, contributing 25.16% to the overall importance, highlighting its crucial role in regulating the temperature and water evaporation processes [31]. Interestingly, Lu et al. [31] found that shortwave radiation is the most significant environmental variable affecting the global GPP, due to its essential function in driving photosynthesis by providing solar energy at the top of the atmosphere. The discrepancy between the Tibetan Plateau and the global situation could be attributed to the fact that shortwave radiation is not the primary factor influencing the GPP on the Tibetan Plateau. Supporting this, Ma et al. [47] noted that, among seven light use efficiency (LUE) models on the Tibetan Plateau, only two suggested that radiation was as influential as water and the temperature in determining the GPP, with the remaining models considering either the temperature or water as the dominant factors. Additionally, Figure 11 reveals that srad (15.60%), shum (13.51%), and wind (11.02%) are also significant contributors, as they collectively influence the temperature and precipitation, which are closely associated with longwave radiation.

The specific humidity, which represents the moisture content of the air, serves as a composite indicator influenced by both the temperature and precipitation. It plays a crucial role in GPP by regulating plant transpiration. Typically, lower specific humidity can increase the transpiration rates; however, when the humidity levels fall too low, plants may close their stomata to conserve water, resulting in reduced photosynthesis [48]. Additionally, as shown in Figure 11, CO₂ contributes 6.27% to the overall importance, significantly impacting the GPP on the Tibetan Plateau, which is consistent with the findings of Li et al. [49]. The rising atmospheric CO₂ concentration enhances the efficiency of light energy and water use by vegetation, thereby promoting plant growth in this region [50]. In the alpine grassland ecosystems of the Tibetan Plateau, studies on the CO₂ flux dynamics and plant-limiting factors have shown that the interplay between water and the thermal conditions is a key determinant of GPP. In humid regions, increasing temperatures can boost photosynthesis and carbon fixation in plants. Conversely, in arid regions, higher temperatures may exacerbate soil moisture evaporation, intensifying drought stress on plants and consequently reducing ecosystem productivity. Overall, despite the fact that elevated CO₂ levels generally have a positive effect on GPP in the Tibetan Plateau, this effect is moderated by various environmental factors, including the hydrological conditions, temperature, and atmospheric dryness. In short, these factors collectively and interactively shape the trends in vegetation productivity within this unique and sensitive ecosystem.

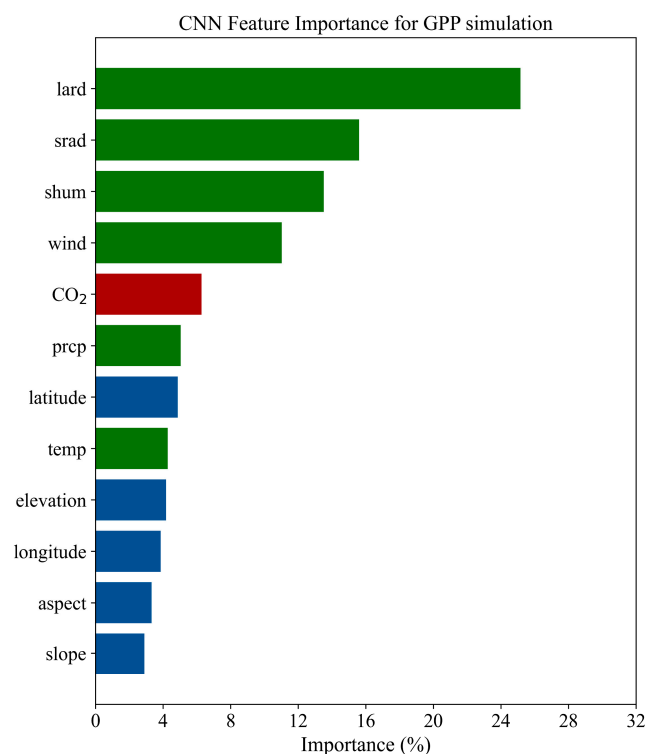


Figure 11. The importance of environmental factors for the GPP simulation.

5.2. Comparison with Prior Studies

In recent years, significant progress has been made in the estimation of GPP on the Tibetan Plateau. Liao et al. [51] analyzed six common remote sensing GPP products (GLASS, MODIS MOD17A2, FLUXCOM, VODCA2, an improved EC-LUE dataset, and VPM data) for the Tibetan Plateau. The results indicated that the MOD17A2 GPP was the lowest, at $484.04 \text{ Tg C} \cdot \text{year}^{-1}$, while GLASS and VODCA2 produced the highest and most similar estimates, at 827.78 and $827.20 \text{ Tg C} \cdot \text{year}^{-1}$, respectively. The improved EC-LUE, VPM, and FLUXCOM GPP estimates fell between these values, at 714.55 , 634.00 , and $587.86 \text{ Tg C} \cdot \text{year}^{-1}$, respectively. Ma et al. [52] reported that the annual GPP across the entire Plateau ranged from 575 to $703 \text{ Tg C} \cdot \text{year}^{-1}$, showing a significant upward trend from 1982 to 2013. In this study, the GPP NIRv data indicated average annual GPP of $790.28 \text{ Tg C} \cdot \text{year}^{-1}$ for the Tibetan Plateau from 1982 to 2018. This estimate lies between the highest values of GLASS and VODCA2 (827.78 and $827.20 \text{ Tg C} \cdot \text{year}^{-1}$, respectively) and the improved EC-LUE ($714.55 \text{ Tg C} \cdot \text{year}^{-1}$), suggesting that the data used in this study are reliable.

Although significant progress has been made in global GPP prediction, there is a noticeable gap in studies specifically focused on the Tibetan Plateau. Most of the existing studies have concentrated on large-scale projections. For example, Schlund et al. [53] applied an ML approach to reduce the uncertainties in the GPP estimates derived from CMIP5, predicting that the global GPP could increase by 39% by the end of the 21st century under the RCP 8.5 scenario. Similarly, Huang et al. [30] analyzed the future global GPP trends using datasets from 18 ESMs in CMIP6, showing an overall increase in GPP across all four SSP scenarios, with the ssp585 scenario indicating the most substantial growth. In another study, Lu et al. [31] projected that, by 2100, the annual global GPP could reach 115.122 Pg C , 116.537 Pg C , 117.626 Pg C , and 120.097 Pg C under the four SSP scenarios. Furthermore, Lu et al. [15] employed a deep learning approach to integrate GPP data from 23 CMIP6 models, producing a high-precision monthly GPP dataset with a spatial resolution of 0.25° , spanning 1850 to 2100 across four climate scenarios.

In contrast to global studies, research on GPP prediction on the Tibetan Plateau is relatively limited. This research gap underscores the critical need for region-specific

studies, such as the current investigation, which focuses on the Tibetan Plateau. This study presents a comprehensive projection of the annual GPP on the Tibetan Plateau under four SSP scenarios. In 2021, the estimated GPP values were 1008.264 Tg C, 992.754 Tg C, 989.377 Tg C, and 998.812 Tg C under ssp126, ssp245, ssp370, and ssp585, respectively. By 2100, these values are projected to shift to 1011.986 Tg C, 1032.679 Tg C, 1044.358 Tg C, and 1055.504 Tg C, reflecting changes of 3.722 Tg C, 39.925 Tg C, 54.980 Tg C, and 56.691 Tg C, respectively, which correspond to percentage changes of 0.36%, 4.02%, 5.55%, and 5.67%. In comparison, Lu et al. [31] indicated increases of 1.67%, 3.29%, 4.22%, and 6.05% for the same scenarios by the end of the century for the global GPP prediction. A comparison of the GPP projections for the global scale and the Tibetan Plateau reveals that the findings of this study are reasonable. These findings highlight the possible changes in vegetation productivity on the Tibetan Plateau under different climate scenarios, providing valuable insights for future ecological and environmental planning in this sensitive region.

5.3. Limitations

This study forecasts the seasonal and annual GPP from 2021 to 2100 across four SSP scenarios using a CNN model to identify significant relationships between environmental factors and GPP. However, challenges remain in understanding the biochemical mechanisms through which environmental changes impact vegetation growth. Nutrient availability is crucial for vegetation growth but has not been considered in the development of more effective ML models. The accuracy of GPP forecasts is largely dependent on the quality of the input data, with potential discrepancies arising from the GPP NIRv dataset, which relies on satellite-based near-infrared reflectance and may not accurately capture the historical GPP. Additionally, the inherent uncertainty in future climate projections complicates GPP predictions, as even advanced ESMs struggle to accurately simulate future climatic conditions. The vegetation dynamics in the region are likely influenced by a combination of climatic and human factors. Human activities, including afforestation and ecological restoration, can enhance GPP and improve vegetation's carbon sequestration capacity, contributing to the goals of "carbon peaking" and "carbon neutrality". Studies suggest that the contributions of climate and human activities to GPP increases are comparable, accounting for 48–56% and 44–52%, respectively [54]. Future research should focus on the interactions between natural processes and anthropogenic influences on vegetation growth on the Tibetan Plateau.

Integrating physical models with ML approaches to simulate GPP presents a promising avenue to enhance the predictive accuracy and understanding of vegetation dynamics. Physical models, grounded in ecological and biological principles, provide a mechanistic understanding of the processes influencing GPP, including photosynthesis, respiration, and nutrient cycling. On the other hand, ML models excel in capturing complex, non-linear relationships within large datasets, making them highly effective in identifying patterns and trends that may not be apparent through traditional modeling approaches. By combining these two methodologies as a physics-informed ML model [55,56], one can leverage the strengths of each, using physical models to inform the structure and parameters of ML algorithms, while employing ML to refine and improve the physical model predictions based on empirical data. This hybrid approach can also enhance the ability to incorporate diverse data sources, including remote sensing, ground-based measurements, and historical climate records, thereby enhancing the predictive power of GPP simulations. Additionally, integrating these methodologies may facilitate a more comprehensive understanding of the interactions between environmental factors, vegetation dynamics, and anthropogenic influences. Future studies should explore specific frameworks and case studies that exemplify this integration, ultimately contributing to more robust and adaptable models for the prediction of GPP in diverse ecological conditions.

6. Conclusions

This study successfully utilized a CNN model to predict the impacts of 21st-century climate change on the GPP in the Tibetan Plateau. By comprehensively considering environmental factors, including climate variables, CO₂ concentrations, and topographical attributes, the CNN model demonstrated outstanding performance in simulating historical GPP data, showcasing excellent robustness. This validates its robustness and reliability in predicting future changes in GPP.

This study forecasted GPP variations under four different SSP scenarios, and the key findings are as follows. (1) The predictions indicate a general increasing trend in GPP for the Tibetan Plateau throughout the 21st century across all scenarios examined, except ssp126. Notably, under the ssp585 scenario, the GPP is projected to rise significantly, potentially reaching annual global GPP of 1050.307 Tg C by 2100, reflecting a 5.67% increase relative to the 2021 levels. (2) A seasonal analysis indicates a pronounced increase in GPP during spring and autumn, likely linked to the temperature conditions, which extend the growing season for plants. (3) An elevation band between 3000 and 4500 m was identified as particularly sensitive to climate change, showing a marked GPP response. (4) Significant GPP increases would occur in the Eastern Tibetan Plateau, including the Qilian Mountains and the upper reaches of the Yellow and Yangtze Rivers. (5) Future research directions should emphasize the potential of integrating physical models with ML approaches to enhance the GPP prediction accuracy.

This study concludes that the potential for GPP increments under climate change conditions is limited; therefore, enhancing human intervention is crucial to achieving carbon neutrality objectives. The findings provide scientific support for the formulation of ecological conservation and carbon management strategies that are responsive to climate change.

Author Contributions: Conceptualization, M.L.; data curation, M.L. and W.R.; formal analysis, M.L.; funding acquisition, W.R.; investigation, M.L.; methodology, W.R.; project administration, W.R.; resources, M.L. and Z.Z.; software, M.L., Z.Z. and W.R.; supervision, W.R.; validation, M.L. and W.R.; visualization, M.L., W.R. and Y.W.; writing—original draft, M.L.; writing—review and editing, Z.Z., W.R. and Y.W. All authors have read and agreed to the published version of the manuscript.

Funding: This research was funded by the National Natural Science Foundation of China (Grant No. 42101406).

Data Availability Statement: The original data presented in the study are openly available at <https://data.tpdc.ac.cn/en/disallow/9bee808a-2dcc-4dc4-be5a-600a464c0e6f> (accessed on 30 September 2024).

Acknowledgments: The authors would like to thank the editors and the reviewers for their crucial comments and suggestions, which improved the quality of this paper.

Conflicts of Interest: The authors declare no conflicts of interest.

References

1. Piao, S.L.; Zhang, X.Z.; Wang, T.; Liang, E.Y.; Wang, S.P.; Zhu, J.T.; Niu, B. Responses and feedback of the Tibetan Plateau's alpine ecosystem to climate change. *Chin. Sci. Bull.* **2019**, *64*, 2842–2855. [\[CrossRef\]](#)
2. Beer, C.; Reichstein, M.; Tomelleri, E.; Ciais, P.; Jung, M.; Carvalhais, N.; Rödenbeck, C.; Arain, M.A.; Baldocchi, D.; Bonan, G.B.; et al. Terrestrial gross carbon dioxide uptake: Global distribution and covariation with climate. *Science* **2010**, *329*, 834–838. [\[CrossRef\]](#)
3. Yuan, W.; Liu, S.; Yu, G.; Bonnefond, J.-M.; Chen, J.; Davis, K.; Desai, A.R.; Goldstein, A.H.; Gianelle, D.; Rossi, F.; et al. Global estimates of evapotranspiration and gross primary production based on MODIS and global meteorology data. *Remote Sens. Environ.* **2010**, *114*, 1416–1431. [\[CrossRef\]](#)
4. Ahlström, A.; Raupach, M.R.; Schurgers, G.; Smith, B.; Arneth, A.; Jung, M.; Reichstein, M.; Canadell, J.G.; Friedlingstein, P.; Jain, A.K.; et al. The dominant role of semi-arid ecosystems in the trend and variability of the land CO₂ sink. *Science* **2015**, *348*, 895–899. [\[CrossRef\]](#)
5. Friedlingstein, P.; Jones, M.W.; O'Sullivan, M.; Andrew, R.M.; Hauck, J.; Peters, G.P.; Peters, W.; Pongratz, J.; Sitch, S.; Le Quéré, C.; et al. Global carbon budget 2019. *Earth Syst. Sci. Data* **2019**, *11*, 1783–1838. [\[CrossRef\]](#)
6. Höhne, N.; Elzen, M.D.; Rogelj, J.; Metz, B.; Fransen, T.; Kuramochi, T.; Olhoff, A.; Alcamo, J.; Winkler, H.; Fu, S.; et al. Emissions: World has four times the work or one-third of the time. *Nature* **2020**, *579*, 25–28. [\[CrossRef\]](#)

7. Fawcett, A.A.; Iyer, G.C.; Clarke, L.E.; Edmonds, J.A.; Hultman, N.E.; McJeon, H.C.; Rogelj, J.; Schuler, R.; Alsalam, J.; Asrar, G.R.; et al. Can Paris pledges avert severe climate change? *Science* **2015**, *350*, 1168–1169. [\[CrossRef\]](#)
8. Hilker, T.; Hall, F.G.; Tucker, C.J.; Coops, N.C.; Black, T.A.; Nichol, C.J.; Sellers, P.J.; Barr, A.; Hollinger, D.Y.; Munger, J.W. Data assimilation of photosynthetic light-use efficiency using multi-angular satellite data: II model implementation and validation. *Remote Sens. Environ.* **2012**, *121*, 287–300. [\[CrossRef\]](#)
9. Zhang, Z.; Xin, Q.; Li, W. Machine learning-based modeling of vegetation leaf area index and gross primary productivity across North America and comparison with a process-based model. *J. Adv. Model. Earth Syst.* **2021**, *13*, e2021MS002802. [\[CrossRef\]](#)
10. Li, W.-P.; Zhang, Y.-W.; Mu, M.; Shi, X.-L.; Zhou, W.-Y.; Ji, J.-J. Spatial and temporal variations of gross primary production simulated by land surface model BCC_AVIM2. *0. Adv. Clim. Change Res.* **2023**, *14*, 286–299. [\[CrossRef\]](#)
11. Zhang, S.; Zhang, J.; Bai, Y.; Koju, U.A.; Igbawua, T.; Chang, Q.; Zhang, D.; Yao, F. Evaluation and improvement of the daily boreal ecosystem productivity simulator in simulating gross primary productivity at 41 flux sites across Europe. *Ecol. Model.* **2018**, *368*, 205–232. [\[CrossRef\]](#)
12. Hajima, T.; Watanabe, M.; Yamamoto, A.; Tatebe, H.; Noguchi, M.A.; Abe, M.; Ohgaito, R.; Ito, A.; Yamazaki, D.; Okajima, H.; et al. Development of the MIROC-ES2L Earth system model and the evaluation of biogeochemical processes and feedbacks. *Geosci. Model. Dev.* **2020**, *13*, 2197–2244. [\[CrossRef\]](#)
13. Hu, Q.; Li, T.; Deng, X.; Wu, T.; Zhai, P.; Huang, D.; Fan, X.; Zhu, Y.; Lin, Y.; Xiao, X.; et al. Intercomparison of global terrestrial carbon fluxes estimated by MODIS and Earth system models. *Sci. Total. Environ.* **2022**, *810*, 152231. [\[CrossRef\]](#)
14. Zhang, C.; Qi, W.; Dong, J.; Deng, Y. How the CMIP6 climate models project the historical terrestrial GPP in China. *Int. J. Clim.* **2022**, *42*, 9449–9461. [\[CrossRef\]](#)
15. Lu, J.; Wang, G.; Feng, D.; Noon, I.K. Improving the Gross Primary Production Estimate by Merging and Downscaling Based on Deep Learning. *Forests* **2023**, *14*, 1201. [\[CrossRef\]](#)
16. Yan, H.; Ran, Q.; Hu, R.; Xue, K.; Zhang, B.; Zhou, S.; Zhang, Z.; Tang, L.; Che, R.; Pang, Z.; et al. Machine learning-based prediction for grassland degradation using geographic, meteorological, plant and microbial data. *Ecol. Indic.* **2022**, *137*, 108738. [\[CrossRef\]](#)
17. Guo, R.; Chen, T.; Chen, X.; Yuan, W.; Liu, S.; He, B.; Li, L.; Wang, S.; Hu, T.; Yan, Q.; et al. Estimating global GPP from the plant functional type perspective using a machine learning approach. *J. Geophys. Res. Biogeosci.* **2023**, *128*, e2022JG007100. [\[CrossRef\]](#)
18. Shanguan, W.; Xiong, Z.L.; Nourani, V.; Li, Q.L.; Lu, X.J.; Li, L.; Huang, F.N.; Zhang, Y.; Sun, W.Y.; Dai, Y.J. A 1 km Global Carbon Flux Dataset Using In Situ Measurements and Deep Learning. *Forests* **2023**, *14*, 913. [\[CrossRef\]](#)
19. Yao, Y.; Wang, X.; Li, Y.; Wang, T.; Shen, M.; Du, M.; He, H.; Li, Y.; Luo, W.; Ma, M.; et al. Spatiotemporal pattern of gross primary productivity and its covariation with climate in China over the last thirty years. *Glob. Change Biol.* **2018**, *24*, 184–196. [\[CrossRef\]](#)
20. Pei, Y.; Dong, J.; Zhang, Y.; Yang, J.; Zhang, Y.; Jiang, C.; Xiao, X. Performance of four state-of-the-art GPP products (VPM, MOD17, BESS and PML) for grasslands in drought years. *Ecol. Inform.* **2020**, *56*, 101052. [\[CrossRef\]](#)
21. Tian, Z.K.; Yi, C.X.; Fu, Y.Y.; Kutter, E.; Krakauer, N.Y.; Fang, W.; Zhang, Q.; Luo, H. Fusion of Multiple Models for Improving Gross Primary Production Estimation with Eddy Covariance Data Based on Machine Learning. *J. Geophys. Res. Biogeosci.* **2023**, *128*, e2022JG007122. [\[CrossRef\]](#)
22. Wang, H.; Shao, W.; Hu, Y.; Cao, W.; Zhang, Y. Assessment of Six Machine Learning Methods for Predicting Gross Primary Productivity in Grassland. *Remote Sens.* **2023**, *15*, 3475. [\[CrossRef\]](#)
23. Ren, W.; Zhu, Z.; Wang, Y.; Su, J.; Zeng, R.; Zheng, D.; Li, X. Comparison of Machine Learning Models in Simulating Glacier Mass Balance: Insights from Maritime and Continental Glaciers in High Mountain Asia. *Remote Sens.* **2024**, *16*, 956. [\[CrossRef\]](#)
24. Ma, J.; Xiao, X.; Miao, R.; Li, Y.; Chen, B.; Zhang, Y.; Zhao, B. Trends and controls of terrestrial gross primary productivity of China during 2000–2016. *Environ. Res. Lett.* **2019**, *14*, 084032. [\[CrossRef\]](#)
25. Tang, Y.; Xu, X.; Zhou, Z.; Qu, Y.; Sun, Y. Estimating global maximum gross primary productivity of vegetation based on the combination of MODIS greenness and temperature data. *Ecol. Inform.* **2021**, *63*, 101307. [\[CrossRef\]](#)
26. Hou, H.; Zhou, B.; Pei, F.; Hu, G.; Su, Z.; Zeng, Y.; Zhang, H.; Gao, Y.; Luo, M.; Li, X. Future land use/land cover change has nontrivial and potentially dominant impact on global gross primary productivity. *Earth's Future* **2022**, *10*, e2021EF002628. [\[CrossRef\]](#)
27. Zhang, Y.; Piao, S.; Sun, Y.; Rogers, B.M.; Li, X.; Lian, X.; Liu, Z.; Chen, A.; Peñuelas, J. Future reversal of warming-enhanced vegetation productivity in the Northern Hemisphere. *Nat. Clim. Change* **2022**, *12*, 581–586. [\[CrossRef\]](#)
28. Xu, C.; McDowell, N.G.; Fisher, R.A.; Wei, L.; Sevanto, S.; Christoffersen, B.O.; Weng, E.; Middleton, R.S. Increasing impacts of extreme droughts on vegetation productivity under climate change. *Nat. Clim. Change* **2019**, *9*, 948–953. [\[CrossRef\]](#)
29. Yan, M.; Yue, X.; Zhou, B.; Sun, X.; Xin, N. Projected changes of ecosystem productivity and their responses to extreme heat events in northern Asia. *Front. Earth Sci.* **2022**, *10*, 970296. [\[CrossRef\]](#)
30. Huang, L.; Zhu, Z.; Huang, M.; Zhao, Q.; Ma, W.; Zeng, H. Projection of gross primary productivity change of global terrestrial ecosystem in the 21st century based on optimal ensemble averaging of CMIP6 models. *Adv. Clim. Change Res.* **2021**, *17*, 514–524.
31. Lu, Q.; Liu, H.; Wei, L.; Zhong, Y.; Zhou, Z. Global prediction of gross primary productivity under future climate change. *Sci. Total. Environ.* **2024**, *912*, 169239. [\[CrossRef\]](#) [\[PubMed\]](#)
32. Boonman, C.C.; Huijbregts, M.A.; Benítez-López, A.; Schipper, A.M.; Thuiller, W.; Santini, L. Trait-based projections of climate change effects on global biome distributions. *Divers. Distrib.* **2022**, *28*, 25–37. [\[CrossRef\]](#)
33. LeCun, Y.; Bengio, Y.; Hinton, G. Deep learning. *Nature* **2015**, *521*, 436–444. [\[CrossRef\]](#)

34. Wang, S.; Zhang, Y.; Ju, W.; Qiu, B.; Zhang, Z. Tracking the seasonal and inter-annual variations of global gross primary production during last four decades using satellite near-infrared reflectance data. *Sci. Total. Environ.* **2021**, *755*, 142569. [\[CrossRef\]](#)
35. Piao, S.L.; Ciais, P.; Huang, Y.; Shen, Z.H.; Peng, S.S.; Li, J.S.; Zhou, L.P.; Liu, H.Y.; Ma, Y.C.; Ding, Y.H.; et al. The impacts of climate change on water resources and agriculture in China. *Nature* **2010**, *467*, 43–51. [\[CrossRef\]](#)
36. Deng, M.; Meng, X.; Lu, Y.; Li, Z.; Zhao, L.; Niu, H.; Chen, H.; Shang, L.; Wang, S.; Sheng, D. The response of vegetation to regional climate change on the Tibetan Plateau based on remote sensing products and the dynamic global vegetation model. *Remote Sens.* **2022**, *14*, 3337. [\[CrossRef\]](#)
37. Jiang, Y.; Yang, K.; Qi, Y.; Zhou, X.; He, J.; Lu, H.; Li, X.; Chen, Y.; Li, X.; Zhou, B.; et al. TPHiPr: A long-term (1979–2020) high-accuracy precipitation dataset (1/30°, daily) for the Third Pole region based on high-resolution atmospheric modeling and dense observations. *Earth Syst. Sci. Data* **2023**, *15*, 621–638. [\[CrossRef\]](#)
38. Cao, B.; Gruber, S.; Zheng, D.; Li, X. The ERA5-Land soil temperature bias in permafrost regions. *Cryosphere* **2020**, *14*, 2581–2595. [\[CrossRef\]](#)
39. Eyring, V.; Bony, S.; Meehl, G.A.; Senior, C.A.; Stevens, B.; Stouffer, R.J.; Taylor, K.E. Overview of the coupled model intercomparison project phase 6 (CMIP6) experimental design and organization. *Geosci. Model. Dev.* **2016**, *9*, 1937–1958. [\[CrossRef\]](#)
40. Stouffer, R.J.; Eyring, V.; Meehl, G.A.; Bony, S.; Senior, C.; Stevens, B.; Taylor, K.E. CMIP5 scientific gaps and recommendations for CMIP6. *Bull. Am. Meteorol. Soc.* **2017**, *98*, 95–105. [\[CrossRef\]](#)
41. Wang, S.; Zhang, Y.; Ju, W.; Chen, J.M.; Ciais, P.; Cescatti, A.; Sardans, J.; Janssens, I.A.; Wu, M.; Berry, J.A. Recent global decline of CO₂ fertilization effects on vegetation photosynthesis. *Science* **2020**, *370*, 1295–1300. [\[CrossRef\]](#) [\[PubMed\]](#)
42. Cheng, W.; Dan, L.; Deng, X.; Feng, J.; Wang, Y.; Peng, J.; Tian, J.; Qi, W.; Liu, Z.; Zheng, X. Global monthly gridded atmospheric carbon dioxide concentrations under the historical and future scenarios. *Sci. Data* **2022**, *9*, 83. [\[CrossRef\]](#) [\[PubMed\]](#)
43. Conrad, O.; Bechtel, B.; Bock, M.; Dietrich, H.; Fischer, E.; Gerlitz, L.; Wehberg, J.; Wichmann, V.; Böhner, J. System for automated geoscientific analyses (SAGA) v. 2.1.4. *Geosci. Model. Dev.* **2015**, *8*, 1991–2007. [\[CrossRef\]](#)
44. Rolf, E. Evaluation challenges for geospatial ML. ICLR 2023 Workshop on Machine Learning for Remote Sensing. *arXiv* **2023**. [\[CrossRef\]](#)
45. You, Y.; Wang, S.; Ma, Y.; Wang, X.; Liu, W. Improved modeling of gross primary productivity of Alpine Grasslands on the Tibetan Plateau using the biome-BGC model. *Remote Sens.* **2019**, *11*, 1287. [\[CrossRef\]](#)
46. Zhou, Z.; Ding, Y.; Shi, H.; Cai, H.; Fu, Q.; Liu, S.; Li, T. Analysis and prediction of vegetation dynamic changes in China: Past, present and future. *Ecol. Indic.* **2020**, *117*, 106642. [\[CrossRef\]](#)
47. Ma, M.; Yuan, W. Model differences in gross primary production on the Qinghai-Tibet-Plateau. *J. Remote Sens. Technol.* **2017**, *32*, 406–418.
48. Grossiord, C.; Buckley, T.N.; Cernusak, L.A.; Novick, K.A.; Poulter, B.; Siegwolf, R.T.; Sperry, J.S.; McDowell, N.G. Plant responses to rising vapor pressure deficit. *New Phytol.* **2020**, *226*, 1550–1566. [\[CrossRef\]](#)
49. Li, J.; Jia, K.; Zhao, L.; Tao, G.; Zhao, W.; Liu, Y.; Yao, Y.; Zhang, X. An Improved Gross Primary Production Model Considering Atmospheric CO₂ Fertilization: The Qinghai-Tibet Plateau as a Case Study. *Remote Sens.* **2024**, *16*, 1856. [\[CrossRef\]](#)
50. Zhu, Z.; Wang, H.; Harrison, S.P.; Prentice, I.C.; Qiao, S.; Tan, S. Optimality principles explaining divergent responses of alpine vegetation to environmental change. *Glob. Change Biol.* **2022**, *29*, 126–142. [\[CrossRef\]](#)
51. Liao, W.J.; Jiao, Y.; Li, S.X.; Hu, Z.M.; Bai, L. Comparative analysis of gross primary productivity in the Qinghai-Tibet Plateau based on long-time series of remote sensing products. *Chin. J. Ecol.* **2024**, *43*, 1859–1869.
52. Ma, M.; Yuan, W.; Dong, J.; Zhang, F.; Cai, W.; Li, H. Large-scale estimates of gross primary production on the Qinghai-Tibet plateau based on remote sensing data. *Int. J. Digit. Earth* **2018**, *11*, 1166–1183. [\[CrossRef\]](#)
53. Schlund, M.; Eyring, V.; Camps-Valls, G.; Friedlingstein, P.; Gentile, P.; Reichstein, M. Constraining uncertainty in projected gross primary production with machine learning. *J. Geophys. Res. Biogeosci.* **2020**, *125*, e2019JG005619. [\[CrossRef\]](#)
54. Chen, Y.; Feng, X.; Tian, H.; Wu, X.; Gao, Z.; Feng, Y.; Piao, S.; Lv, N.; Pan, N.; Fu, B. Accelerated increase in vegetation carbon sequestration in China after 2010: A turning point resulting from climate and human interaction. *Glob. Change Biol.* **2021**, *27*, 5848–5864. [\[CrossRef\]](#) [\[PubMed\]](#)
55. Li, X.; Feng, M.; Ran, Y.; Su, Y.; Liu, F.; Huang, C.; Shen, H.; Xiao, Q.; Su, J.; Yuan, S.; et al. Big Data in Earth system science and progress towards a digital twin. *Nat. Rev. Earth Environ.* **2023**, *4*, 319–332. [\[CrossRef\]](#)
56. Ren, W.; Li, X.; Zheng, D.; Zeng, R.; Su, J.; Mu, T.; Wang, Y. Enhancing flood simulation in data-limited glacial river basins through hybrid modeling and multi-source remote sensing data. *Remote Sens.* **2023**, *15*, 4527. [\[CrossRef\]](#)

Disclaimer/Publisher’s Note: The statements, opinions and data contained in all publications are solely those of the individual author(s) and contributor(s) and not of MDPI and/or the editor(s). MDPI and/or the editor(s) disclaim responsibility for any injury to people or property resulting from any ideas, methods, instructions or products referred to in the content.